Published in final edited form as:

J Control Release. 2016 October 28; 240: 312–322. doi:10.1016/j.jconrel.2016.01.004.

Recent Advances of Semiconducting Polymer Nanoparticles in In Vivo Molecular Imaging

Kanyi Pu[a,b], **Niladri Chattopadhyay**[a], and **Jianghong Rao**[a,*]

[a]Molecular Imaging Program at Stanford Department of Radiology School of Medicine, Stanford University, USA

[b]School of Chemical and Biomedical Engineering, Nanyang Technological University, Singapore, 637457

Abstract

Semiconducting polymer nanoparticles (SPNs) emerge as attractive molecular imaging nanoagents in living animals because of their excellent optical properties including large absorption coefficients, tunable optical properties and controllable dimensions, high photostability, and the use of organic and biologically inert components without toxic metals. This review summarizes the recent advances of these new organic nanoparticles in in vivo molecular imaging. The in vivo biocompatibility of SPNs is discussed first in details, followed by examples of their applications ranging from sentinel lymph node mapping and tumor imaging to long-term cell tracking, to drug toxicity and bacterial infection imaging for fluorescence, bioluminescence, chemiluminescence and photoacoustic imaging in living animals. The utility of SPNs for designing smart activatable probes for real-time in vivo imaging is also discussed.

Graphical abstract

* jrao@stanford.edu.

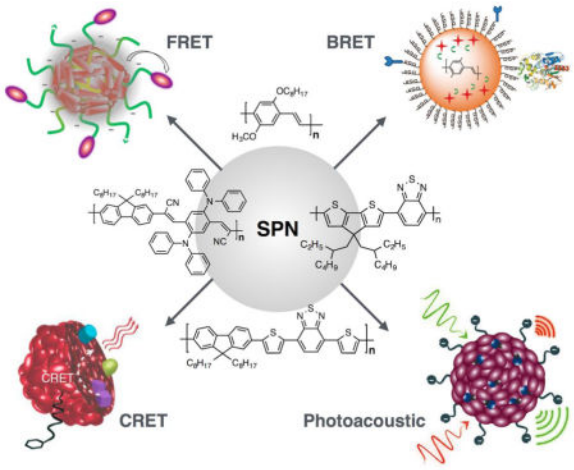

1. Introduction

Non-invasive molecular imaging enables visualization of biological molecules and their interactions in living systems in real time at various levels from molecules and single cells, to tissues, and organs within living subjects.[1, 2] Information obtained through molecule imaging has greatly expanded our knowledge of biology and medicine, and empowered our ability in detecting and treating life-threatening diseases.[3–5] Molecular imaging involves specialized instrumentation and frequently uses imaging agents to noninvasively and longitudinally probe tissue characteristics and/or biomarkers.[6, 7] Among numerous imaging gents, nanoparticles have been extensively investigated and proven to be effective for biomedical imaging because of their multimodal signaling capacity, enhanced targeting capability *via* multivalent binding, enhanced permeation and retention for tumor targeting, large payload delivery and tunable biodistribution profiles.[8–11] The convergence of molecular imaging and nanotechnology is providing new opportunities to better understand fundamental biology, monitor health, perform diagnosis and treat diseases.

Among nanoparticles, optical nanomaterials such as semiconductor quantum dots (QDs),[12, 13] up-conversion nanoparticles,[14–17] dye-embedded silica nanoparticles,[18] carbon dots,[19] metal nanoclusters [20] and dye-doped polymer nanoparticles [21] have formed a large collection of imaging agents and contributed to the advance of molecular imaging. As a recent addition to this class of imaging agents, semiconducting polymer nanoparticles (SPNs) have gained growing attention because of their attractive optical properties. SPNs are primarily made from semiconducting polymers (SPs) that are optically and electronically active polymers with many applications ranging from electronic devices [22, 23] and sensors [24, 25] to tissue engineering.[26] SPs have π-electron delocalized backbones, and their formation of spherical nanoparticles results from collapse of hydrophobic polymer chains owing to substantial decrease in solvent hydrophobicity upon going from organic solvents to water.[27–30] In addition to their large absorption coefficients, tunable optical properties and controllable dimensions, the completely organic and biologically inert components of SPNs represent another advantage, which intrinsically circumvents the issue of heavy metal

ion-induced toxicity to living organisms and thus potentially possess good biocompatibility.[31–33]

The preparation methods, optical properties and bioconjugation chemistry of SPNs have been widely studied,[32, 34–36] and their biological applications have been demonstrated for *in vitro* sensing,[37–40] bioorthogonal labeling,[41] specific cellular and subcellular imaging,[29, 42–44] drug and gene delivery,[45, 46] and antimicrobial,[47, 48] as examined in a number of recent reviews.[21, 27, 28, 30, 31, 33, 49–53] This short review article will instead focus on recent advances of SPNs as molecular imaging probes in living animals. We will first discuss the *in vivo* toxicological study of a typical SPN developed by us, and then highlight the *in vivo* imaging applications of SPNs for several optical imaging modalities including fluorescence, chemi-/bioluminescence and photoacoustic (PA) imaging.

2. Biocompatibility

Poly(*p*-phenylenevinylene) (PPV) derivatives (P1–P3), poly(fluorene-*alt*-benzothiadiazole) (PFBT) derivatives (P5–P8), a poly(*p*-phenyleneethynylene) (PPE) derivative (P9), a poly(fluorenyldivinylene) (PFV) derivative (P10), and other SPs (P10–P12) have been transformed into nanoparticles and used for fluorescence imaging in living mice. Given the increasing number of applications of SPNs, several in vitro studies have been reported.[54–57] However, there have been limited in vivo toxicology studies to fully examine the biocompatibility of these nanoparticles.

A recent in vitro study conducted by Ye et al. [56] evaluated the toxicity and oxidative stress induced by semiconducting polymer dots in RAW264.7 mouse macrophages. Using a series of assays evaluating cell viability (MTT and trypan blue), proliferation (propidium iodide based flow cytometry) and necrosis as well as fluorescence based assays to measure oxidative stress to the cells the authors demonstrate that toxicity is dose dependent and significantly lower as compared to equivalent doses of quantum dots. Of note in this study is the observation that SPNs caused higher cardiolipin peroxidation than quantum dots at the higher concentrations tested (~30 μg/mL – 120 μg/mL) which warrants further investigation. Overall, these studies indicate favorable in vitro biocompatibility of SPNs; however, future studies with longer incubations as well as using primary human hepatocytes would offer further information on biocompatibility. In a first step towards assessing the interaction of SPNs with human derived primary cells, Abelha et al. demonstrated using human blood from healthy volunteers that stealth SPN formulations exhibiting neutrally charged, pegylated surfaces do not stimulate platelet activation or aggregation,[58] but may induce a low degree of hemolysis in the presence of free surfactant and can inhibit physiological mediators of platelet aggregation, such as ADP.

Recently, Feng et al. evaluated the impact of SPNs on epididymal mouse sperm from 7–8 weeks old balb/c mice, and found no significant differences in either sperm viability or fertilization rate even with a high concentration of the SPNs ((~0.3 mg/mL).[59] However, long-term embryonic development studies were not conducted and such studies will be important for advanced toxicological characterisation of promising SPNs.

We have conducted acute toxicological analysis of SPNs under development in our laboratory. This study demonstrates the first systematic toxicity evaluation of SPNs following intravenous injection into mice. As reported previously,[60] SPN-P8 comprised of P8, and a galactosylated graft copolymer of poly(styrene) and poly(ethylene glycol) (PS-*g*-PEG-Gal), was synthesized by nanoprecipitation method, and its average diameter measured by dynamic light scattering (DLS) is ~50 nm. We injected 5–6 week old balb/c mice with 0.8 mg of the SPNs *via* a tail vein catheter. To study impact of acute exposure of living animals to this nanomaterial, blood was drawn *via* cardiac puncture at 1, 4 or 14 days post injection (n=5 in each group) and assessed by complete blood chemistry, liver and kidney function tests.

The dose for the toxicity studies was determined by a pre-clinically useful dose as established recently for imaging drug-induced hepatotoxicity in living animals.[60] Control animals were injected with saline. This strain of mice was selected as compared to nude mice in order to identify responses in animals with a fully functional immune system that may be missed in T-cell deficient nude mice. In this study, single, intravenous, administration of 0.8 mg of SPN-P8 were overall well tolerated by the subjects. Upon injection, and throughout the entire study, no unusual behavior or differences between treatment groups were observed, including vocalizations, labored breathing, difficulties moving, hunching or unusual interactions with cage mates.

The SPNs did not lead to acute or chronic toxicity in balb/c mice, but some transient changes in blood counts were observed which returned to normal levels by day 4 or 14 of the study (Fig. 1). Specifically, the MCV counts were lower in SPN-P8 treated mice than control mice. Lower MCV counts indicate that RBCs are smaller in size, primarily caused by iron deficiency. However, MCH values (indicator of oxygen-carrying haemoglobin) & haemoglobin values were not significantly different than values observed in control mice. Taken together these results suggest no significant impact on hematopoiesis. While WBCs counts were normal over the entire study duration, a closer look at the WBC differential count indicates that there was a transient increase in neutrophils accompanied by a transient decrease in lymphocytes at day 1 but returning to normal levels by day 4 and remaining stable through day 14 post-exposure of SPN-P8. The observed altered population changes as detected by blood cytometry analysis reveals a transient inflammatory process that may be considered a normal host response to the presence of foreign materials introduced into the bloodstream. Similar results have been observed with other classes of nanomaterials such as iron oxide magnetite nanoparticles.[61, 62] Differential WBC counts should be included in future toxicological characterization of promising SPNs to ensure that the initial host response does not persist beyond 24 h post-treatment.

Since injected nanoparticles are rapidly cleared by the reticuloendothelial system – liver function tests were conducted at each time point (Fig. 1g–i). We observed, transient elevations in aspartate aminotransferase (AST) and alanine aminotransferase (ALT) at day 1 following administration of the SPNs; however, the levels returned to normal within 1–4 days post injection and these experiments were repeated in an additional cohort of 5 animals to confirm findings. Such transient elevations in liver enzymes have previously been noted not only with iron oxide nanoparticles but also with administration of saline [61]. Dan et al.

evaluated the toxicity of SPN-P7 in healthy, non-tumor bearing ICR mice at a single time-point (7 days post-injection of SPNs) and observed no alterations in ALT or AST values as compared to saline injected control animals.[63] The kidney function tests were normal throughout the entire duration of the study (Fig. 1m–o). Careful and extensive necropsy did not reveal gross abnormalities or abnormal organ weights. Further, tissues (liver, spleen, lung and heart) assessed via immunohistochemistry staining demonstrated no histopathological alterations as compared to control (Fig. 2).

Because of the relatively small number of animals and a single dose of SPNs, our findings should be considered as a pilot study. Although more extensive series are needed to confirm our results, these encouraging results support further exploration of SPNs in biomedical applications in living animals.

3. Fluorescence Imaging

Cyano substituted, poly(*p*-phenylenevinylene) (CN-PPVs) (P1–P3, Scheme 1) based SPNs were synthesized through in-situ colloidal Knoevenagel polymerization and applied for sentinel lymph node (SLN) mapping in living mice.[64] After intradermal injection of those SPNs into the forepaw pad of mice, the nanoparticles drained rapidly from the interstitial site of injection into the lymphatics and arrived at an axillary node in around 1 min, permitting real-time SLN mapping. However, as only a small portion of the injected dose reached the SLNs with the majority retained at the injection site, the injection site had the strong signal that potentially interfered with the signal from SLNs. To alleviate this issue, the CN-PPV nanoparticles were doped with a photoswitching dye (1,2-bis(2,4-dimethyl-5-phenyl- 3-thienyl)-3,3,4,4,5,5-hexafluoro-1-cyclopentene, BTE) (Scheme 2) to endow the SPN with the photoswitchable ability. Improved signal-to-background contrast was achieved as SLNs were selectively switched on while the remnant nanoparticles at the injection site remained dark.[65]

Fluorescent SPNs that made of fluorescence resonance energy transfer (FRET) backbone structures (P5, P7–P9) have also been reported for tumor imaging in living mice. A 2011 paper reports the conjugation of chlorotoxin (a 36-amino acid peptide that binds preferentially to glioma cells) to the surface of the SPNs composed of P5 and P6 mixture and application of this nanoconjugate to image the medulloblastoma tumor xenografts in brain.[66] However, only *ex vivo* images have been reported, probably because the strong light scattering of skull and the short excitation wavelengths of P5 and P6 make *in vivo* imaging less effective. Another group reported a folate-modified P7-based SPN and verified its targeting capability in the subcutaneous H22 tumor mice model.[63] Instead of preparing SPNs by co-precipitation method, an amphiphilic pentablock SP (P9) was designed and synthesized to be able to self-assemble into nanoparticles in aqueous solution for targeted imaging of KB tumors in living mice.[67] Due to the short excitation wavelength (465 nm), real-time imaging of the nanoparticles in mice by whole animal fluorescence imaging was not enabled but ex vivo imaging conducted 24 h post-injection that showed strong fluorescence in tumors.

We recently reported SPN-based *in vivo* cell tracking by taking advantage of their good biocompatibility and photostability.[68] To improve the cellular uptake, we synthesized a phosphorylcholine-coated P8-based SPN (*p*SPN-P8) that allowed it to enter cells within 0.5 h in complete culture medium (Fig. 3a&3b). Cell uptake of this *p*SPN-P8 was found not to obviously depend on specific cell surface receptors since the murine stromal MS-5 cells, the adenocarcinoma HeLa cells and the primary human renal cell carcinoma (RCC) cells were rapidly and efficiently labeled with *p*SPN-P8. The rapid and efficient internalization of the SPN was attributed to its surface coating with phosphorylcholine groups that had strong binding to the cell membrane and facilitated endocytosis. The capability of *p*SPN-P8 for long-term in vitro cell tracking was evidenced by the fact that almost all cells maintained fluorescent even after cell growth for 5 days. In addition, the *p*SPN-P8 permits cell tracking of RCC cells in living mice at a lower limit of detection of 10,000 cells with no obvious intensity loss after 12 days (Fig. 3c&3d). Histological analysis showed that the presence of *p*SPN-P8 had little influence on the phenotypes and genotypes of RCC, demonstrating the suitability of SPNs for long-term, efficient cell labeling agents.

Incorporation of other optically active dyes into SPNs can lead to smart activatable nanoprobes for imaging of chemical mediators or biomarkers in disease sites in living animals. We recently developed a nanoprobe based on SPN (SPN-P10) for the detection of reactive oxygen and nitrogen species (RONS),[69] a hallmark of many pathological processes ranging from acute and chronic bacterial infections to chronic diseases such as cancer, cardiovascular disease, and arthritis.[70, 71] The nanoprobe comprises a RONS-inert SPN core (P10, energy donor, Scheme 1) covered by RONS-sensitive fluorophore molecules (IR775S, energy acceptor, Scheme 2),[72] enabling FRET from the SPN core to the fluorophore in the absence of RONS (Fig. 4a).[69] The presence of RONS can decompose the energy-accepting fluorophore (IR775S) and subsequently abolish the FRET within SPN-P10, leading to ratiometric fluorescence response toward RONS. For instance, with increasing concentrations of $ONOO^-$, the emission peak at 678 nm correspondingly increased with the concurrent loss of emission at 818 nm (Fig. 4b). The probe emission at 678 nm can be significantly enhanced by $ONOO^-$ (4.0 times), ClO^- (3.6 times) and $^{\bullet}OH$ (2.5 times), and slightly enhanced by $^1O_2$ (1.4 times), $O_2^{\bullet -}$ (1.3 times) and NO (1.2 times), but not by H_2O_2.

As SPN-P10 has a ratiometric signal toward RONS, hyperspectral *in vivo* fluorescence imaging was employed to deconvolve unactivated from activated probe states in live animals (Fig. 4c). Note that difference between the *in vivo* and *in vitro* spectra was caused by a decreased sensitivity of the charge-coupled device (CCD) camera of the *in vivo* imager in the near-infrared region. SPN-P10 was used to detect RONS in spontaneous *Corynebacterium bovis* (*C. bovis*) bacterial infection. As shown in Fig. 4d&4e, SPN-P10 first specifically accumulated in the infected foci within 15 min through the EPR effect, and then was progressively induced to change from unactivated (pseudo-green) to activated (pseudo-red) states by microenvironmental RONS in the bacterial infection regions, with complete probe activation by 60 min. Therefore, this design potentially provides more accurate spatial resolution for *in vivo* RONS imaging as compared with ‘off-on’ imaging probes that can only be seen once activated.

Similarly, other activatable nanoprobes can be designed by doping SPNs. For example, a SPN-based hypoxia imaging probe was developed by incorporating the P11 (Scheme 1) core with a NIR phosphorescent oxygen-sensitive dye (meso-tetraphenyl tetrabenzoporphyrin platinum(II), PtBzPor, Scheme 2).[73] After systemic delivery, SPN-P11 passively targeted diseases including tumor, ischemia and arthritis. Analysis of the ratiometric signals from SPN-P11 in mice allowed for the estimation of the partial oxygen pressure in tumor (~16 mmHg) which was significantly lower than the physiological partial oxygen pressure in liver sinusoid (~45 mmHg).

Although the aforementioned SPN-based fluorescence imaging utilizes the emission wavelength in the near-infrared (NIR) range (650–900 nm) that minimizes the interference from tissue autofluorescence, it still faces light scattering. It has been shown that second-near-infrared window (SNIR, 1000–1700 nm) optical imaging affords comparably low absorbance and tissue autofluorescence as the conventional NIR-I (650–900 nm) but up to a 1,000-fold greater reduction in scattering losses.[74–78] Recently, Dai's group at Stanford developed SPNs that are able to emit light in the SNIR window and applied them for ultrafast hemodynamic imaging in living mice.[79] In particular, P12-based SPN (Scheme 1) has a higher fluorescence quantum yield (~1.7%) as compared to carbon nanotube (~0.4%), which results in the high spatial and time-resolved imaging of the blood flow pattern in cardiogram waveform over a single cardiac cycle (~200 ms) of a mouse. This work indicates the great potential of SPNs in SNIR fluorescence imaging.

4. Bioluminescence and Chemiluminescence

Bioluminescence resonance energy transfer (BRET) provides a useful way to bypass tissue autofluorescence and enhance detection sensitivity and specificity.[80, 81] To improve the optical imaging of SPNs, we recently developed self-luminescing NIR SPNs by integrating BRET and FRET in an energy transfer relay to enable self-luminescing NIR emission (Fig. 5).[82] In this BRET/FRET system, the BRET donor and acceptor are *R. reniformis luciferase* (Luc8) and P4 (Scheme 1), respectively; while the FRET donor and acceptor are P4 and NIR775 (Scheme 2), respectively. The bioluminescence spectrum of this nanoparticles is shown in Fig. 5b, which proves the occurrence of efficient relay energy transfer relay from Luc8 to P4 and to NIR775. Conjugation of cyclic-RGD peptide as the targeting ligand to this SPN permitted targeted tumor imaging. As shown in Fig. 5c, strong bioluminescence signals can be detected in the U87MG tumor of the mice 5 min after intravenous injection; in comparison, the fluorescence signal in the U87MG tumor is much weaker. Moreover, bioluminescence imaging provides the excellent tumor-to-background ratio (~100) for imaging very small tumors (2–3 mm in diameter), which is ~30-fold better than fluorescence imaging (Fig. 5d). The use of BRET/FRET relay greatly expands the use of SPN for optical imaging, allowing for bioluminescence imaging at the near infrared wavelength with the same bioluminescent protein *Renila* luciferase.

In addition to using bioluminescence as the signal to track the in vivo location of nanoparticles, we recently integrated chemiluminescence property into SPNs for real-time imaging of drug-induced liver damage in living mice.[60] Although drug toxicity is a longstanding concern in modern medicine,[83] current drug-safety assays for hepatotoxicity

use biomarkers with low predictive power.[84] The production of RONS has been proposed as an early unifying event linking the bioactivation of drugs to hepatotoxicity and as a more direct and mechanistic indicator of hepatotoxic potential.[85] Accordingly, we designed a SPN that uses chemiluminescence resonance energy transfer (CRET) and FRET to respectively detect H_2O_2 and peroxynitrite ($ONOO^-$)/hypochlorite (^-OCl) (Fig. 6a). We incorporated a chemiluminescent substrate (bis-(2,4,5-trichloro-6-(pentyloxycarbonyl)phenyl)oxalate (CPPO, Scheme 2) into the SP (P8, Scheme 1) matrix that can react with H_2O_2 to generate luminescence without external light excitation *via* CRET. To improve the hepatocyte uptake, the surface of SPN was modified with galactose to bind the asialoglycoprotein receptor expressed on the sinusoidal membrane of hepatocytes.[86] In this CRET/FRET SPN, the core P8 serves as both the FRET energy donor and the CRET energy acceptor, while the cyanine dye, IR775SH, irreversibly decomposes in the presence of ($ONOO^-$)/hypochlorite (^-OCl) owing to the oxidative cleavage of its polymethine linkers,[72] leading to abolished FRET and thus ratiometric signals.

The CRET/FRET SPN effectively detected drug-induced hepatotoxicity and its remediation longitudinally in mice after systemic challenge with drugs such as the analgesic and anti-pyretic acetaminophen (APAP) and the anti-tuberculosis agent isoniazid. Moreover, dose-dependent RONS activity in the liver was detected within minutes of drug challenge (Fig. 6b), which preceded histological changes, protein nitration and DNA double-strand-break induction. The CRET/FRET SPN also allowed the mechanistic study of drug-induced liver toxicity. The mechanism for APAP bioactivation involves CYP450-mediated oxidation to an iminoquinone, *N*-acetylparaquinonimine (NAPQI), which can bind directly to cellular proteins to induce mitochondrial dysfunction and the production of superoxide ($O^{2\bullet-}$) and $ONOO^-$ or undergo reduction by molecular oxygen to directly form $O^{2\bullet-}$ and H_2O_2.[87] Using the antioxidant (glutathione, GSH) and the CYP450 inhibitors (1-aminobenzotriazole (1-ABT) and *trans*-1,2-dichloroethylene (*t*-1,2-DCE)), a reduction of chemiluminescence emission and of the fluorescence index from the SPN with all three of these inhibitors were observed (Fig. 6c&6d), which indicated successful remediation of oxidative and nitrosative stress, respectively. This example shows that SPNs can be developed into effective probes to detect drug-induced toxicity and monitor remediation outcome, potentially contributing to improving drug development processes.

5. Photoacoustic imaging

Photoacoustic (PA) imaging, a new nonionizing imaging technology that integrates optical excitation with ultrasonic detection based on the PA effect,[88] provides deeper tissue imaging penetration with a higher spatial resolution when compared with traditional optical imaging techniques (e.g. fluorescence). Despite the promise of PA imaging in biology and medicine, full utilization of its potential heavily relies on the development of efficient PA agents. By now, small-molecule organic dyes,[89, 90] fluorescent proteins,[91, 92] metallic nanoparticles,[93–99] carbon nanotubes,[100, 101] two-dimensional graphene analogues [102–105] and porphysomes [106–108] have been studied as exogenous contrast agents. Development of imaging agents has already contributed to facilitate the application PA imaging in monitoring anatomic and physiological changes in diseases, and continues to be active in molecular imaging.

Recently, we have transformed photovoltaic SPs (P13&P14, Scheme 1) into PA agents that have a unique set of advantages including a large mass extinction coefficient and high photostability.[109] SPN-P13 provides stronger (on a per mass basis) and more photostable PA signals in the NIR region when compared with single-wall carbon nanotubes (SWNTs) and gold nanorods (GNRs). At the same mass concentration, the PA amplitude of SPN-P13 at 700 nm was more than five times that of SWNTs and GNRs, effectively reducing their detection limit (2 μg/mL) in living mice relative to both SWNTs and GNRs (9 μg/mL). This enhanced sensitivity can decrease the dosing levels for *in vivo* PA imaging applications, as proven by PA imaging of major lymph nodes in living mice with a high signal-to-noise ratio of 13.3 after a single low-dose (50 μg) intravenous administration of SPN-P13.

The synthetic and structural flexibility of SPNs permitted the further development of SPN-P13 into an activatable NIR ratiometric photoacoustic probe (RSPN-P13) for *in vivo* RONS imaging (Fig. 7a). As SPN-P13 itself has high stability towards RONS, we doped it with IR775SH to afford a ratiometric photoacoustic probe in a way that is similar to the FRET design for SPN-P10. The initial PA spectrum of RSPN-P13 showed three maxima at 700, 735 and 820 nm (Fig. 7b), with nearly the same amplitude. In the presence of $ONOO^-$ and/or ClO^-, the PA peak at 735 nm decreased significantly while that at 820 nm almost disappeared, but the peak at 700 nm remained nearly the same (Fig. 7b). In contrast, in the presence of other RONS, the PA spectrum remained essentially unchanged. RSPN-P13 was able to longitudinally detect the generation of RONS in a murine model of zymosan-induced acute oedema (Fig. 7c). The PA ratiometric signal enhancements of RSPN-P13 was 25, 7.3 and 2.7 times in solution, in cells, and in living mice, respectively, comparable to values reported for fluorescence probes.[110]

Two other SPs have also been reported for PA imaging. Polypyrrole (P15, Scheme 1) based SPNs were prepared from in-situ chemical oxidation polymerization,[111] and another group synthesized P16 (Scheme 1) and then formulated P15 into the SPN through nanoprecipitation.[112] Both examples demonstrated their application in enhanced PA imaging of brain vasculature after intravenous administration of SPNs. SPN-P15 was further integrated for magnetic resonance imaging (MRI) and X-ray computed tomography (CT) modality through conjugation of gadolinium chelates to the surface and encapsulation of Tantalum Oxide, respectively.[113, 114] By virtue of the photothermal conversion ability of P15, both dual-modal SPNs could be used for thermal ablation of tumor under NIR laser irradiation. These studies demonstrate the potential of SPNs for multimodality imaging and imaging-guided photothermal therapy.

6. Conclusions

SPNs have many intrinsic advantages such as good biocompatibility, excellent photostability and oxidative tolerance for *in vivo* molecular imaging, as demonstrated by the studies summarized in this review. These properties are crucial for imaging in living animals but do not all exist in other optical imaging agents such as small-molecule dyes and metallic nanoparticles (such as QDs and gold nanorods). As the optical properties of SPNs are mainly determined by the precursor SPs, they are not dependent on the nanoparticle size, which differentiates SPNs from many of the metallic nanoparticles with strongly size-

dependent spectral properties. In addition, sensing and functional moieties can be readily incorporated or encapsulated into SPNs during synthesis, enabling molecular imaging of diseases/biochemical molecules of interests with the imaging modality of choice (such as chemi/bioluminescence, photoacoustic, MRI and X-ray CT), and therapeutic capability (photothermal and photodynamic therapies). SPNs thus represent a multifunctional nanoplatform that facilitates the preclinical investigation of physiological and pathological processes in living subjects.

While SPNs hold great promises for in vivo molecular imaging, there are important issues that should be addressed before their advance to clinical translations. For instance, despite the benign organic components and unnoticeable in vivo toxicity of SPNs in preliminary animal studies, their biodegradability and clearance from the body have to be fully investigated. The long-term biosafety and the excretion of SPNs from the body are largely unclear. For the purpose of potential clinical translation rapid and complete clearance of nanoparticles after imaging is always desirable. SPNs may be potentially synthesized with a size smaller than the physiologic pore size of filtration slit in the glomerular capillary wall (5 nm) so that they can be rapidly cleared out through urinary excretion. Another possible solution is to develop biodegradable SPNs; biodegradable amphiphilic polymers such as poly(lactic-co-glycolic acid) are already available, but SPs that can be degraded in vivo have been less explored and need to be designed specifically. In addition, further reducing the dosage of SPNs can help minimize potential toxicity, particularly for photoacoustic imaging, which requires enhanced signal readouts from SPNs. Thereby, new chemistry for the preparation of ultrasmall, compact, biodegradable and high-performance SPNs is highly demanded for their advance towards clinical applications.

Acknowledgments

We acknowledge the use of the SCi^3 Stanford Small Animal Imaging Core Facility. This work was supported by the NIH National Cancer Institute (NCI) grants R01DK099800, CCNE-T (U54CA119367) and ICMIC (P50CA114747). KP also acknowledges Nanyang Technological University for the start-up grant (NTU-SUG: M4081627.120).

References

1. James ML, Gambhir SS. A molecular imaging primer: modalities, imaging agents, and applications. Physiological Reviews. 2012; 92:897–965. [PubMed: 22535898]
2. Jokerst JV, Gambhir SS. Molecular imaging with theranostic nanoparticles. Accounts Chem Res. 2011; 44:1050–60.
3. Weissleder R. Molecular imaging in cancer. Science. 2006; 312:1168–71. [PubMed: 16728630]
4. Weissleder R, Pittet MJ. Imaging in the era of molecular oncology. Nature. 2008; 452:580–9. [PubMed: 18385732]
5. Osborn EA, Jaffer FA. Advances in molecular imaging of atherosclerotic vascular disease. Current Opinion in Cardiology. 2008; 23:620–8. [PubMed: 18830079]
6. Massoud TF, Gambhir SS. Molecular imaging in living subjects: seeing fundamental biological processes in a new light. Genes & Development. 2003; 17:545–80. [PubMed: 12629038]
7. Kobayashi H, Longmire MR, Ogawa M, Choyke PL. Rational chemical design of the next generation of molecular imaging probes based on physics and biology: mixing modalities, colors and signals. Chem Soc Rev. 2011; 40:4626–48. [PubMed: 21607237]
8. Wagner V, Dullaart A, Bock AK, Zweck A. The emerging nanomedicine landscape. Nature Biotechnology. 2006; 24:1211–7.

9. Choi HS, Liu W, Liu F, Nasr K, Misra P, Bawendi MG, et al. Design considerations for tumour-targeted nanoparticles. Nature Nanotechnology. 2010; 5:42–7.
10. Cheng Z, Al Zaki A, Hui JZ, Muzykantov VR, Tsourkas A. Multifunctional nanoparticles: cost versus benefit of adding targeting and imaging capabilities. Science. 2012; 338:903–10. [PubMed: 23161990]
11. Ng KK, Lovell JF, Zheng G. Lipoprotein-inspired nanoparticles for cancer theranostics. Accounts Chem Res. 2011; 44:1105–13.
12. Michalet X, Pinaud FF, Bentolila LA, Tsay JM, Doose S, Li JJ, et al. Quantum dots for live cells, in vivo imaging, and diagnostics. Science. 2005; 307:538–44. [PubMed: 15681376]
13. Kairdolf BA, Smith AM, Stokes TH, Wang MD, Young AN, Nie S. Semiconductor quantum dots for bioimaging and biodiagnostic applications. Annual Review of Analytical Chemistry. 2013; 6:143–62.
14. Idris NM, Gnanasammandhan MK, Zhang J, Ho PC, Mahendran R, Zhang Y. In vivo photodynamic therapy using upconversion nanoparticles as remote-controlled nanotransducers. Nat Med. 2012; 18:1580–5. [PubMed: 22983397]
15. Yang Y, Shao Q, Deng R, Wang C, Teng X, Cheng K, et al. In vitro and in vivo uncaging and bioluminescence imaging by using photocaged upconversion nanoparticles. Angewandte Chemie International Edition. 2012; 51:3125–9.
16. Liu Y, Chen M, Cao T, Sun Y, Li C, Liu Q, et al. A cyanine-modified nanosystem for in vivo upconversion luminescence bioimaging of methylmercury. Journal of the American Chemical Society. 2013; 135:9869–76. [PubMed: 23763640]
17. Liu X, Yan C-H, Capobianco JA. Photon upconversion nanomaterials. Chem Soc Rev. 2015; 44:1299–301. [PubMed: 25716767]
18. Burns AA, Vider J, Ow H, Herz E, Penate-Medina O, Baumgart M, et al. Fluorescent silica nanoparticles with efficient urinary excretion for nanomedicine. Nano Letters. 2009; 9:442–8. [PubMed: 19099455]
19. Yang S-T, Cao L, Luo PG, Lu F, Wang X, Wang H, et al. Carbon dots for optical imaging in vivo. Journal of the American Chemical Society. 2009; 131:11308. [PubMed: 19722643]
20. Chen L-Y, Wang C-W, Yuan Z, Chang H-T. Fluorescent gold nanoclusters: recent advances in sensing and imaging. Analytical Chemistry. 2015; 87:216–29. [PubMed: 25275676]
21. Peng H-S, Chiu DT. Soft fluorescent nanomaterials for biological and biomedical imaging. Chem Soc Rev. 2015; doi: 10.1039/C4CS00294F
22. Peet J, Kim JY, Coates NE, Ma WL, Moses D, Heeger AJ, et al. Efficiency enhancement in low-bandgap polymer solar cells by processing with alkane dithiols. Nat Mater. 2007; 6:497–500. [PubMed: 17529968]
23. Mei JG, Diao Y, Appleton AL, Fang L, Bao ZN. Integrated materials design of organic semiconductors for field-effect transistors. Journal of the American Chemical Society. 2013; 135:6724–46. [PubMed: 23557391]
24. Sokolov AN, Tee BCK, Bettinger CJ, Tok JBH, Bao ZN. Chemical and engineering approaches to enable organic field-effect transistors for electronic skin applications. Accounts Chem Res. 2012; 45:361–71.
25. Rose A, Zhu Z, Madigan CF, Swager TM, Bulovic V. Sensitivity gains in chemosensing by lasing action in organic polymers. Nature. 2005; 434:876–9. [PubMed: 15829959]
26. Sanghvi AB, Miller KP, Belcher AM, Schmidt CE. Biomaterials functionalization using a novel peptide that selectively binds to a conducting polymer. Nat Mater. 2005; 4:496–502. [PubMed: 15895095]
27. Wu C, Chiu DT. Highly fluorescent semiconducting polymer dots for biology and medicine. Angew Chem Int Ed Engl. 2013; 52:3086–109. [PubMed: 23307291]
28. Zhu C, Liu L, Yang Q, Lv F, Wang S. Water-soluble conjugated polymers for imaging, diagnosis, and therapy. Chem Rev. 2012; 112:4687–735. [PubMed: 22670807]
29. Howes P, Green M, Levitt J, Suhling K, Hughes M. Phospholipid encapsulated semiconducting polymer nanoparticles: their use in cell imaging and protein attachment. J Am Chem Soc. 2010; 132:3989–96. [PubMed: 20175539]

30. Pecher J, Mecking S. Nanoparticles of conjugated polymers. Chem Rev. 2010; 110:6260–79. [PubMed: 20684570]
31. Pu KY, Liu B. Fluorescent conjugated polyelectrolytes for bioimaging. Advanced Functional Materials. 2011; 21:3408–23.
32. Wu C, Szymanski C, McNeill J. Preparation and encapsulation of highly fluorescent conjugated polymer nanoparticles. Langmuir. 2006; 22:2956–60. [PubMed: 16548540]
33. Feng L, Zhu C, Yuan H, Liu L, Lv F, Wang S. Conjugated polymer nanoparticles: preparation, properties, functionalization and biological applications. Chem Soc Rev. 2013; 42:6620–33. [PubMed: 23744297]
34. Wu CF, Szymanski C, Cain Z, McNeill J. Conjugated polymer dots for multiphoton fluorescence imaging. Journal of the American Chemical Society. 2007; 129:12904. [PubMed: 17918941]
35. Howes P, Thorogate R, Green M, Jickells S, Daniel B. Synthesis, characterisation and intracellular imaging of PEG capped BEHP-PPV nanospheres. Chem Commun. 2009:2490–2.
36. Petkau K, Kaeser A, Fischer I, Brunsveld L, Schenning AP. Pre- and postfunctionalized self-assembled pi-conjugated fluorescent organic nanoparticles for dual targeting. J Am Chem Soc. 2011; 133:17063–71. [PubMed: 21913650]
37. Wu CF, Bull B, Christensen K, McNeill J. Ratiometric Single-Nanoparticle Oxygen Sensors for Biological Imaging. Angew Chem Int Edit. 2009; 48:2741–5.
38. Chan YH, Wu CF, Ye FM, Jin YH, Smith PB, Chiu DT. Development of ultrabright semiconducting polymer dots for ratiometric pH sensing. Analytical Chemistry. 2011; 83:1448–55. [PubMed: 21244093]
39. Childress ES, Roberts CA, Sherwood DY, LeGuyader CLM, Harbron EJ. Ratiometric fluorescence detection of mercury ions in water by conjugated polymer nanoparticles. Analytical Chemistry. 2012; 84:1235–9. [PubMed: 22280026]
40. Ye FM, Wu CF, Jin YH, Chan YH, Zhang XJ, Chiu DT. Ratiometric temperature sensing with semiconducting polymer dots. Journal of the American Chemical Society. 2011; 133:8146–9. [PubMed: 21548583]
41. Wu CF, Jin YH, Schneider T, Burnham DR, Smith PB, Chiu DT. Ultrabright and bioorthogonal labeling of cellular targets using semiconducting polymer dots and Click chemistry. Angew Chem Int Edit. 2010; 49:9436–40.
42. Pu K-Y, Li K, Shi J, Liu B. Fluorescent single-molecular core-shell nanospheres of hyperbranched conjugated polyelectrolyte for live-cell imaging. Chem Mater. 2009; 21:3816–22.
43. Wu C, Schneider T, Zeigler M, Yu J, Schiro PG, Burnham DR, et al. Bioconjugation of ultrabright semiconducting polymer dots for specific cellular targeting. J Am Chem Soc. 2010; 132:15410–7. [PubMed: 20929226]
44. Ding D, Pu KY, Li K, Liu B. Conjugated oligoelectrolyte-polyhedral oligomeric silsesquioxane loaded pH-responsive nanoparticles for targeted fluorescence imaging of cancer cell nucleus. Chem Commun. 2011; 47:9837–9.
45. Silva AT, Alien N, Ye C, Verchot J, Moon JH. Conjugated polymer nanoparticles for effective siRNA delivery to tobacco BY-2 protoplasts. Bmc Plant Biology. 2010; 10
46. Feng X, Tang Y, Duan X, Liu L, Wang S. Lipid-modified conjugated polymer nanoparticles for cell imaging and transfection. J Mater Chem. 2010; 20:1312–6.
47. Xing C, Xu Q, Tang H, Liu L, Wang S. Conjugated polymer/porphyrin complexes for efficient energy transfer and improving light-activated antibacterial activity. Journal of the American Chemical Society. 2009; 131:13117–24. [PubMed: 19702260]
48. Feng X, Yang G, Liu L, Lv F, Yang Q, Wang S, et al. A convenient preparation of multi-spectral microparticles by bacteria-mediated assemblies of conjugated polymer nanoparticles for cell imaging and barcoding. Advanced Materials. 2012; 24:637–41. [PubMed: 21932281]
49. Tian ZY, Yu JB, Wu CF, Szymanski C, McNeill J. Amplified energy transfer in conjugated polymer nanoparticle tags and sensors. Nanoscale. 2010; 2:1999–2011. [PubMed: 20697652]
50. Yuan HX, Wang B, Lv FT, Liu LB, Wang S. Conjugated-polymer-based energy-transfer systems for antimicrobial and anticancer applications. Advanced Materials. 2014; 26:6978–82. [PubMed: 24711269]

51. Li K, Liu B. Polymer-encapsulated organic nanoparticles for fluorescence and photoacoustic imaging. Chem Soc Rev. 2014; 43:6570–97. [PubMed: 24792930]
52. Massey M, Wu M, Conroy EM, Algar WR. Mind your P's and Q's: the coming of age of semiconducting polymer dots and semiconductor quantum dots in biological applications. Curr Opin Biotech. 2015; 34:30–40. [PubMed: 25481436]
53. Chan Y-H, Wu P-J. Semiconducting polymer nanoparticles as fluorescent probes for biological imaging and sensing. Particle & Particle Systems Characterization. 2015; 32:11–28.
54. Li K, Pan J, Feng S-S, Wu AW, Pu K-Y, Liu Y, et al. Generic strategy of preparing fluorescent conjugated-polymer-loaded poly(DL-lactide-co-Glycolide) nanoparticles for targeted cell imaging. Advanced Functional Materials. 2009; 19:3535–42.
55. Moon JH, McDaniel W, Maclean P, Hancock LF. Live-cell-permeable poly(p-phenylene ethynylene). Angew Chem Int Ed Engl. 2007; 46:8223–5. [PubMed: 17886818]
56. Ye F, White CC, Jin Y, Hu X, Hayden S, Zhang X, et al. Toxicity and oxidative stress induced by semiconducting polymer dots in RAW264. 7 mouse macrophages. Nanoscale. 2015; 7:10085–93. [PubMed: 25978523]
57. Fernando LP, Kandel PK, Yu J, McNeill J, Ackroyd PC, Christensen KA. Mechanism of cellular uptake of highly fluorescent conjugated polymer nanoparticles. Biomacromolecules. 2010; 11:2675–82. [PubMed: 20863132]
58. Khanbeigi RA, Hashim Z, Abelha TF, Pitchford S, Collins H, Green M, et al. Interactions of stealth conjugated polymer nanoparticles with human whole blood. Journal of Materials Chemistry B. 2015; 3:2463–71.
59. Gang F, Qiang C, Peng Z, Xiaomei W, Guimiao L, Gaixia X, et al. The effect of polymer dots on bioactivity of mouse sperm in vitro. Proceedings of the SPIE - Progress in Biomedical Optics and Imaging. 2014; 9230:92300S, 6–6.
60. Shuhendler AJ, Pu K, Cui L, Uetrecht JP, Rao J. Real-time imaging of oxidative and nitrosative stress in the liver of live animals for drug-toxicity testing. Nat Biotech. 2014; 32:373–80.
61. Jain TK, Reddy MK, Morales MA, Leslie-Pelecky DL, Labhasetwar V. Biodistribution, clearance, and biocompatibility of iron oxide magnetic nanoparticles in rats. Molecular Pharmaceutics. 2008; 5:316–27. [PubMed: 18217714]
62. Freitas MLL, Silva LP, Azevedo RB, Garcia VAP, Lacava LM, Grisolia CK, et al. A double-coated magnetite-based magnetic fluid evaluation by cytometry and genetic tests. Journal of Magnetism and Magnetic Materials. 2002; 252:396–8.
63. Dan D, Jie L, Guangxue F, Kai L, Yong H, Bin L. Bright far-red/near-infrared conjugated polymer nanoparticles for in vivo bioimaging. Small. 2013; 9:3093–102. [PubMed: 23625815]
64. Kim S, Lim C-K, Na J, Lee Y-D, Kim K, Choi K, et al. Conjugated polymer nanoparticles for biomedical in vivo imaging. Chem Commun. 2010; 46:1617–9.
65. Jeong K, Park S, Lee Y-D, Lim C-K, Kim J, Chung BH, et al. Conjugated polymer/photochromophore binary nanococktails: bistable photoswitching of near-infrared fluorescence for in vivo imaging. Advanced Materials. 2013; 25:5574. [PubMed: 23847108]
66. Wu C, Hansen SJ, Hou Q, Yu J, Zeigler M, Jin Y, et al. Design of highly emissive polymer dot bioconjugates for in vivo tumor targeting. Angewandte Chemie International Edition. 2011; 50:3430–4.
67. Ahmed E, Morton SW, Hammond PT, Swager TM. Fluorescent multiblock pi-conjugated polymer nanoparticles for in vivo tumor targeting. Advanced Materials. 2013; 25:4504–10. [PubMed: 23794490]
68. Pu K, Shuhendler AJ, Valta MP, Cui L, Saar M, Peehl DM, et al. Phosphorylcholine-coated semiconducting polymer nanoparticles as rapid and efficient labeling agents for in vivo cell tracking. Advanced Healthcare Materials. 2014; 3:1292–8. [PubMed: 24668903]
69. Pu K, Shuhendler AJ, Rao J. Semiconducting polymer nanoprobe for in vivo imaging of reactive oxygen and nitrogen species. Angewandte Chemie International Edition. 2013; 52:10325–9.
70. Medzhitov R. Origin and physiological roles of inflammation. Nature. 2008; 454:428–35. [PubMed: 18650913]
71. Szabo C, Ischiropoulos H, Radi R. Peroxynitrite: biochemistry, pathophysiology and development of therapeutics. Nat Rev Drug Discov. 2007; 6:662–80. [PubMed: 17667957]

72. Oushiki D, Kojima H, Terai T, Arita M, Hanaoka K, Urano Y, et al. Development and application of a near-infrared fluorescence probe for oxidative stress based on differential reactivity of linked cyanine dyes. Journal of the American Chemical Society. 2010; 132:2795–801. [PubMed: 20136129]
73. Seo YH, Cho MJ, Cheong OJ, Jang W-D, Ohulchanskyy TY, Lee S, et al. Low-bandgap biophotonic nanoblend: A platform for systemic disease targeting and functional imaging. Biomaterials. 2015; 39:225–33. [PubMed: 25465444]
74. Hong G, Diao S, Chang J, Antaris AL, Chen C, Zhang B, et al. Through-skull fluorescence imaging of the brain in a new near-infrared window. Nature Photonics. 2014; 8:723–30. [PubMed: 27642366]
75. Hong G, Lee JC, Jha A, Diao S, Nakayama KH, Hou L, et al. Near-infrared II fluorescence for imaging hindlimb vessel regeneration with dynamic tissue perfusion measurement. Circulation-Cardiovascular Imaging. 2014; 7:517–U150. [PubMed: 24657826]
76. Tao Z, Hong G, Shinji C, Chen C, Diao S, Antaris AL, et al. Biological imaging using nanoparticles of small organic molecules with fluorescence emission at wavelengths longer than 1000 nm. Angew Chem Int Edit. 2013; 52:13002–6.
77. Hong G, Lee JC, Robinson JT, Raaz U, Xie L, Huang NF, et al. Multifunctional in vivo vascular imaging using near-infrared II fluorescence. Nature Medicine. 2012; 18:1841.
78. Kleinfeld D, Mitra PP, Helmchen F, Denk W. Fluctuations and stimulus-induced changes in blood flow observed in individual capillaries in layers 2 through 4 of rat neocortex. Proceedings of the National Academy of Sciences of the United States of America. 1998; 95:15741–6. [PubMed: 9861040]
79. Hong G, Zou Y, Antaris AL, Diao S, Wu D, Cheng K, et al. Ultrafast fluorescence imaging in vivo with conjugated polymer fluorophores in the second near-infrared window. Nat Commun. 2014; 5
80. So M-K, Xu C, Loening AM, Gambhir SS, Rao J. Self-illuminating quantum dot conjugates for in vivo imaging. Nature Biotechnology. 2006; 24:339–43.
81. Xia Z, Rao J. Biosensing and imaging based on bioluminescence resonance energy transfer. Curr Opin Biotech. 2009; 20:37–44. [PubMed: 19216068]
82. Xiong L, Shuhendler AJ, Rao J. Self-luminescing BRET-FRET near-infrared dots for in vivo lymph-node mapping and tumour imaging. Nat Commun. 2012; 3:1193. [PubMed: 23149738]
83. Nasr A, Lauterio TJ, Davis MW. Unapproved drugs in the United States and the Food and Drug Administration. Advances in Therapy. 2011; 28:842–56. [PubMed: 21894470]
84. Sakatis MZ, Reese MJ, Harrell AW, Taylor MA, Baines IA, Chen L, et al. Preclinical strategy to reduce clinical hepatotoxicity using in vitro bioactivation data for > 200 compounds. Chemical Research in Toxicology. 2012; 25:2067–82. [PubMed: 22931300]
85. Walsh, JS.; Miwa, GT. Bioactivation of drugs: risk and drug design. In: Cho, AK., editor. Annual Review of Pharmacology and Toxicology. Vol. 52. 2011. p. 145-67.
86. Hu Y, Haynes MT, Wang Y, Liu F, Huang L. A highly efficient synthetic vector: nonhydrodynamic delivery of DNA to hepatocyte nuclei in vivo. ACS Nano. 2013; 7:5376–84. [PubMed: 23647441]
87. Hinson JA, Roberts DW, James LP. Mechanisms of acetaminophen-induced liver necrosis. Handbook of experimental pharmacology. 2010:369–405. [PubMed: 20020268]
88. Kim C, Favazza C, Wang LHV. In vivo photoacoustic tomography of chemicals: high-resolution functional and molecular optical imaging at new depths. Chem Rev. 2010; 110:2756–82. [PubMed: 20210338]
89. Levi J, Kothapalli SR, Ma TJ, Hartman K, Khuri-Yakub BT, Gambhir SS. Design, Synthesis, and Imaging of an Activatable Photoacoustic Probe. Journal of the American Chemical Society. 2010; 132:11264–9. [PubMed: 20698693]
90. Zhang Y, Cai X, Wang Y, Zhang C, Li L, Choi SW, et al. Noninvasive photoacoustic microscopy of viving cells in two and three dimensions through enhancement by a metabolite dye. Angew Chem Int Edit. 2011; 50:7359–63.
91. Filonov GS, Krumholz A, Xia J, Yao J, Wang LV, Verkhusha VV. Deep-tissue photoacoustic tomography of a genetically encoded near-infrared fluorescent probe. Angew Chem Int Ed Engl. 2012; 51:1448–51. [PubMed: 22213541]

92. Hoffman RM. The multiple uses of fluorescent proteins to visualize cancer in vivo. Nat Rev Cancer. 2005; 5:796–806. [PubMed: 16195751]

93. Song KH, Kim CH, Cobley CM, Xia YN, Wang LV. Near-infrared gold nanocages as a new class of tracers for photoacoustic sentinel lymph node mapping on a rat model. Nano Letters. 2009; 9:183–8. [PubMed: 19072058]

94. Xia YN, Li WY, Cobley CM, Chen JY, Xia XH, Zhang Q, et al. Gold nanocages: from synthesis to theranostic applications. Accounts Chem Res. 2011; 44:914–24.

95. Jin YD, Jia CX, Huang SW, O'Donnell M, Gao XH. Multifunctional nanoparticles as coupled contrast agents. Nat Commun. 2010; 1:41. [PubMed: 20975706]

96. Ku G, Zhou M, Song S, Huang Q, Hazle J, Li C. Copper sulfide nanoparticles as a new class of photoacoustic contrast agent for deep tissue imaging at 1064 nm. ACS Nano. 2012; 6:7489–96. [PubMed: 22812694]

97. Zhou M, Ku G, Pageon L, Li C. Theranostic probe for simultaneous in vivo photoacoustic imaging and confined photothermolysis by pulsed laser at 1064 nm in 4T1 breast cancer model. Nanoscale. 2014; 6:15228–35. [PubMed: 25379880]

98. Liu J, Zheng X, Yan L, Zhou L, Tian G, Yin W, et al. Bismuth sulfide nanorods as a precision nanomedicine for in vivo multimodal imaging-guided photothermal therapy of tumor. ACS Nano. 2015; 9:696–707. [PubMed: 25561009]

99. Chen M, Tang SH, Guo ZD, Wang XY, Mo SG, Huang XQ, et al. Core-Shell Pd@Au nanoplates as theranostic agents for in vivo photoacoustic imaging, CT imaging, and photothermal therapy. Advanced Materials. 2014; 26:8210–6. [PubMed: 25363309]

100. De la Zerda A, Zavaleta C, Keren S, Vaithilingam S, Bodapati S, Liu Z, et al. Carbon nanotubes as photoacoustic molecular imaging agents in living mice. Nat Nanotechnol. 2008; 3:557–62. [PubMed: 18772918]

101. Kim JW, Galanzha EI, Shashkov EV, Moon HM, Zharov VP. Golden carbon nanotubes as multimodal photoacoustic and photothermal high-contrast molecular agents. Nat Nanotechnol. 2009; 4:688–94. [PubMed: 19809462]

102. Cheng L, Liu J, Gu X, Gong H, Shi X, Liu T, et al. PEGylated WS(2) nanosheets as a multifunctional theranostic agent for in vivo dual-modal CT/photoacoustic imaging guided photothermal therapy. Adv Mater. 2014; 26:1886–93. [PubMed: 24375758]

103. Nie L, Huang P, Li W, Yan X, Jin A, Wang Z, et al. Early-stage imaging of nanocarrier-enhanced chemotherapy response in living subjects by scalable photoacoustic microscopy. ACS Nano. 2014; 8:12141–50. [PubMed: 25406986]

104. Yang K, Hu L, Ma X, Ye S, Cheng L, Shi X, et al. Multimodal imaging guided photothermal therapy using functionalized graphene nanosheets anchored with magnetic nanoparticles. Adv Mater. 2012; 24:1868–72. [PubMed: 22378564]

105. Song X-R, Wang X, Yu S-X, Cao J, Li S-H, Li J, et al. Co9Se8 Nanoplates as a new theranostic platform for photoacoustic/magnetic resonance dual-modal-imaging-guided chemo-photothermal combination therapy. Advanced Materials. 2015; 27:3285–91. [PubMed: 25885638]

106. Lovell JF, Jin CS, Huynh E, Jin HL, Kim C, Rubinstein JL, et al. Porphysome nanovesicles generated by porphyrin bilayers for use as multimodal biophotonic contrast agents. Nature Materials. 2011; 10:324–32. [PubMed: 21423187]

107. Huynh E, LeungBen YC, Helfield BL, Shakiba M, Gandier J-A, Jin CS, et al. In situ conversion of porphyrin microbubbles to nanoparticles for multimodality imaging. Nat Nanotechnol. 2015; 10:325–32. [PubMed: 25822929]

108. Zhang Y, Jeon M, Rich LJ, Hong H, Geng J, Zhang Y, et al. Non-invasive multimodal functional imaging of the intestine with frozen micellar naphthalocyanines. Nat Nanotechnol. 2014; 9:631–8. [PubMed: 24997526]

109. Pu K, Shuhendler AJ, Jokerst JV, Mei J, Gambhir SS, Bao Z, et al. Semiconducting polymer nanoparticles as photoacoustic molecular imaging probes in living mice. Nat Nanotechnol. 2014; 9:233–9. [PubMed: 24463363]

110. Dickinson BC, Chang CJ. Chemistry and biology of reactive oxygen species in signaling or stress responses. Nat Chem Biol. 2011; 7:504–11. [PubMed: 21769097]

111. Zha Z, Deng Z, Li Y, Li C, Wang J, Wang S, et al. Biocompatible polypyrrole nanoparticles as a novel organic photoacoustic contrast agent for deep tissue imaging. Nanoscale. 2013; 5:4462–7. [PubMed: 23584573]

112. Liu J, Geng J, Liao L-D, Thakor N, Gao X, Liu B. Conjugated polymer nanoparticles for photoacoustic vascular imaging. Polymer Chemistry. 2014; 5:2854–62.

113. Yushen J, Yanyan L, Xibo M, Zhengbao Z, Liangliang S, Jie T, et al. Encapsulating tantalum oxide into polypyrrole nanoparticles for X-ray CT/photoacoustic bimodal imaging-guided photothermal ablation of cancer. Biomaterials. 2014; 35:5795–804. [PubMed: 24746966]

114. Liang X, Li Y, Li X, Jing L, Deng Z, Yue X, et al. PEGylated polypyrrole nanoparticles conjugating gadolinium chelates for dual-modal MRI/photoacoustic imaging guided photothermal therapy of cancer. Advanced Functional Materials. 2015; 25:1451–62.

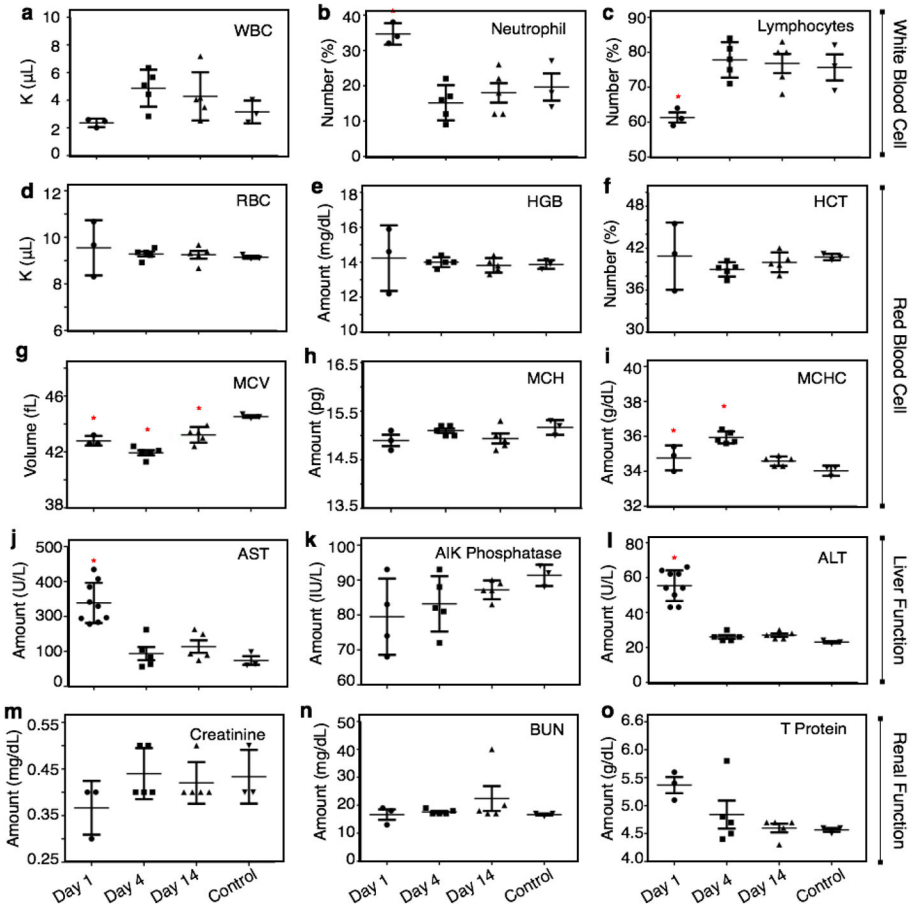

Fig. 1.

(**a–c**) White blood counts of balb/c mice following injection of SPN-P8. Mean with SEM of white blood cell (WBC) numbers (**a**), percentage of neutrophils among white blood cells (**b**), percentage of lymphocytes among white blood cells (**c**). (**d–i**) Red blood counts of balb/c mice following injection of SPN-P8. Mean with SEM of red blood cell (RBC) numbers (**d**), hemoglobin (HGB) content (**e**), hematocritmean (HCT) content (**f**), mean corpuscular volume (MCV) (**g**), corpuscular hemoglobin (MCH) (**h**) or mean corpuscular hemoglobin concentration (MCHC) (**i**). (**j–l**) Liver function test results of balb/c mice following injection of SPN-P8. Mean with SEM of aspartate aminotransferase (AST) numbers (**j**), alkaline phosphatase (**k**) or alanine aminotransferase (ALT) (**l**). (**m–o**) Renal function test results of balb/c mice following injection of SPN-P8. Mean with SEM of creatine (**m**), blood urea nitrogen (BUN) numbers (**n**) or total protein (T protein) (**o**). Each group had 3–5 balb/c mice per group. Each group had 3–5 balb/c mice per group. Data are plotted over a period of 14 days following injection of SPN-P8 or saline (control). Data for AST and ALT were repeated in a cohort of 5 animals to confirm findings. Statistically significant differences (p<0/05) are indicated with an asterisk.

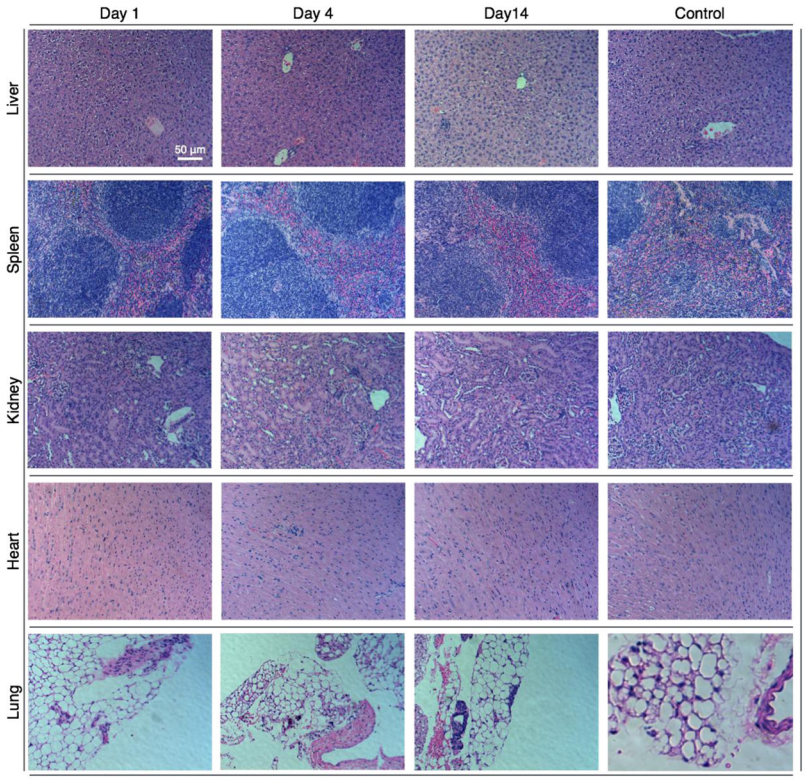

Fig. 2.

Histology of liver, spleen, kidney, heart and lung harvested at day 1, 4, and 14 after intravenous injection of the SPN-P8. Haematoxylin and eosin (H&E) stains of tissue sections of organs isolated from balb/c mice injected with saline or a single dose of SPN-P8 (0.8 mg). No cellular or tissue damage was observed over 14 days of the toxicology study. These samples were scored independently by a veterinary pathologist at Stanford veterinary pathology laboratory.

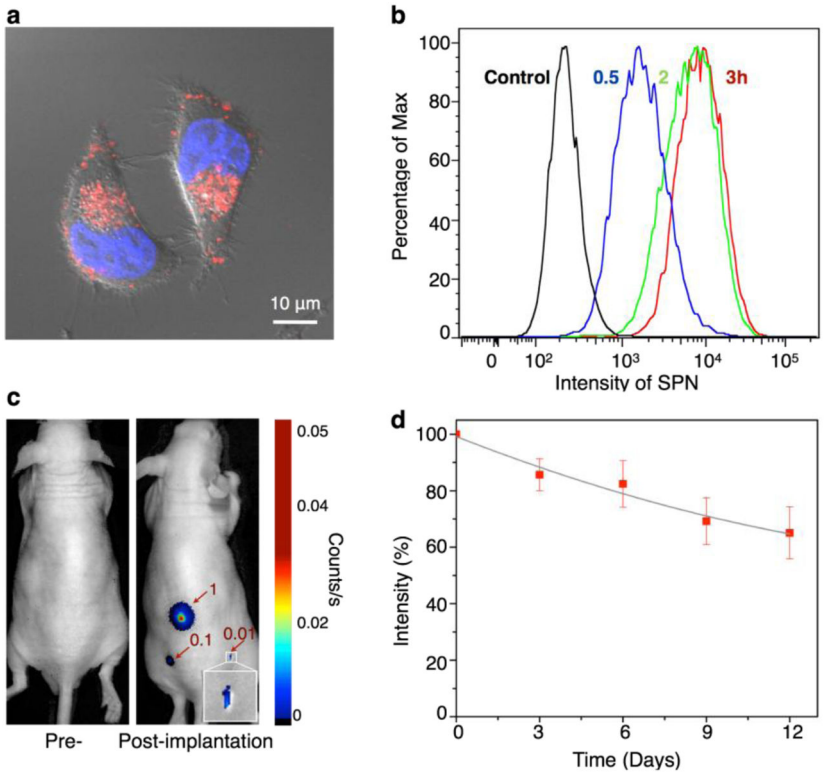

Fig. 3.

(**a**) Confocal laser scanning microscopy images of living HeLa cells after incubation with *p*SPN-P8 at 37 °C for 3 h. The cell nuclei were stained with Hoechst 33342 (blue). (**b**) Flow cytometry profiles of HeLa cells after incubation with *p*SPN-P8 at 37 °C for 0.5, 2 or 3h. (**c**) Fluorescence images of a mouse before (left) and 10 min after (right) subcutaneous implantation with 1×10^6 (1), 1×10^5 (0.1), and 1×10^4 (0.01) primary human RCC cells pre-labeled with *p*SPN-P8. (**d**) Quantification of fluorescence intensities of the implanted cells as a function of post-implantation time. Intensity (%) stands for the percentage of the intensity at the indicated day relative to the initial value. Reproduced from ref. 68.

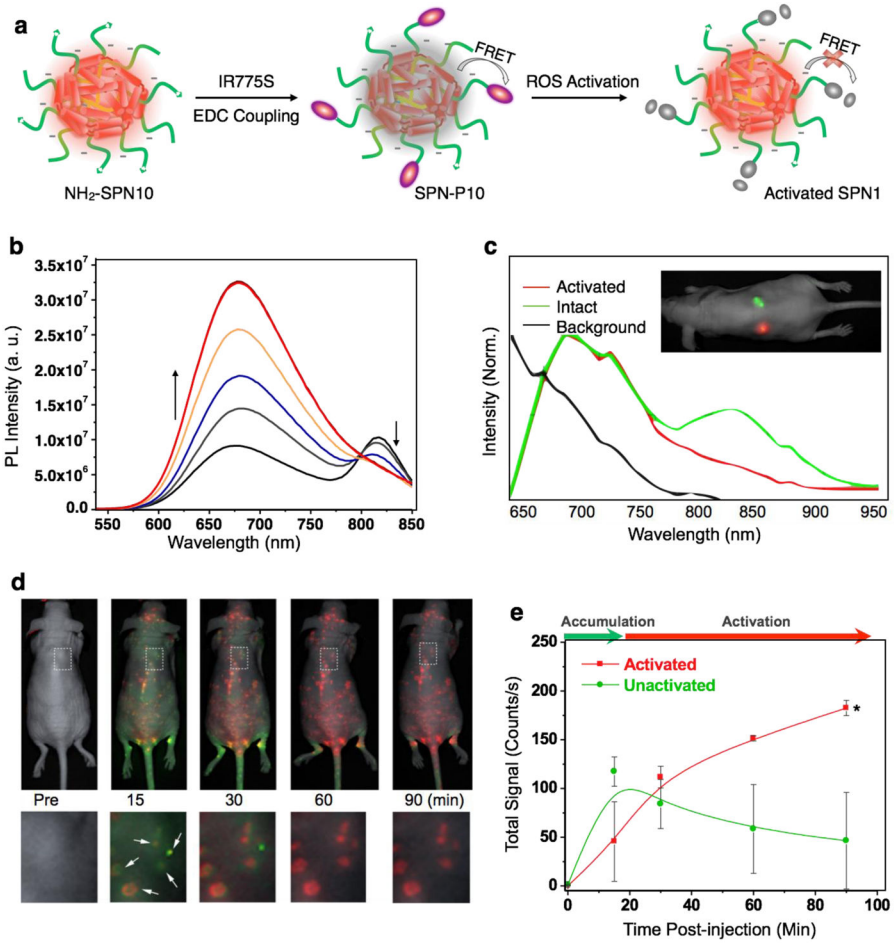

Fig. 4.

(**a**) Schematic of the preparation and RONS sensing of SPN-P10. (**b**) Fluorescence spectra of SPN-P10 in PBS (30 mM, pH = 7.4) in the absence or presence of $ONOO^-$ with concentrations ranging from 0 to 0.5 μM at intervals of 0.1 μM. (**c**) Unactivated (green) and preactivated SPN-P10 (red) were injected subcutaneously into the back of a nude mouse, followed by fluorescence hyperspectral imaging to record the in vivo spectra of the activated (red) and unactivated probes (green), as well as autofluorescence (black). (**d**) Imaging RONS with SPN-P10 in mice with spontaneous systemic C. *bovis* bacterial infection. Overlaid images of activated (red) and unactivated (green) SPN-P10 following i.v. administration to mice with spontaneous bacterial infections (n=4). Enlargements of the regions indicated by dashed white boxes are given below each corresponding image. White arrows indicate localized regions of bacterial infection. (d) Quantification of activated (red) and non-activated (green) SPN-P10 fluorescence over time. †Significantly different change in fluorescence between unactivated and activated nanoprobe ($p<0.05$). Reproduced from ref. 69.

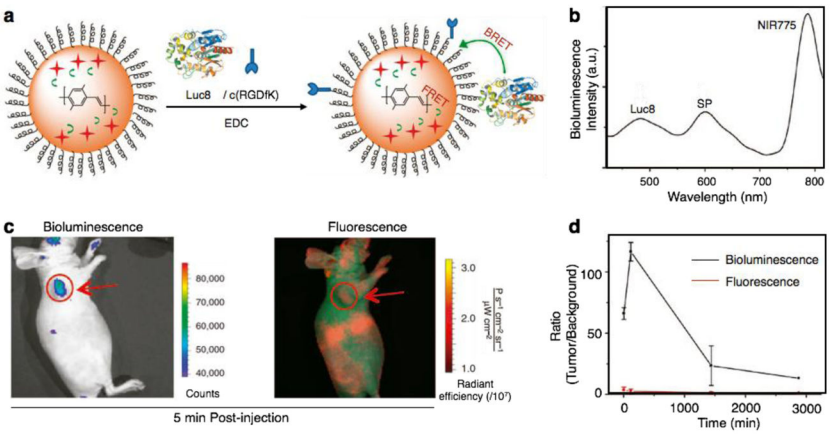

Fig. 5.

(**a**) Schematic of self-luminescing BRET-FRET SPN. (**b**) Bioluminescence emission spectrum of SPN in PBS buffer. (**c**) In vivo bioluminescence and fluorescence imaging of U87MG tumors in mice after intravenous injection of SPN for 5 mins. (**d**) ROI analysis of the bioluminescence and fluorescence intensity between tumor and background of mice over time. Reproduced from ref. 82.

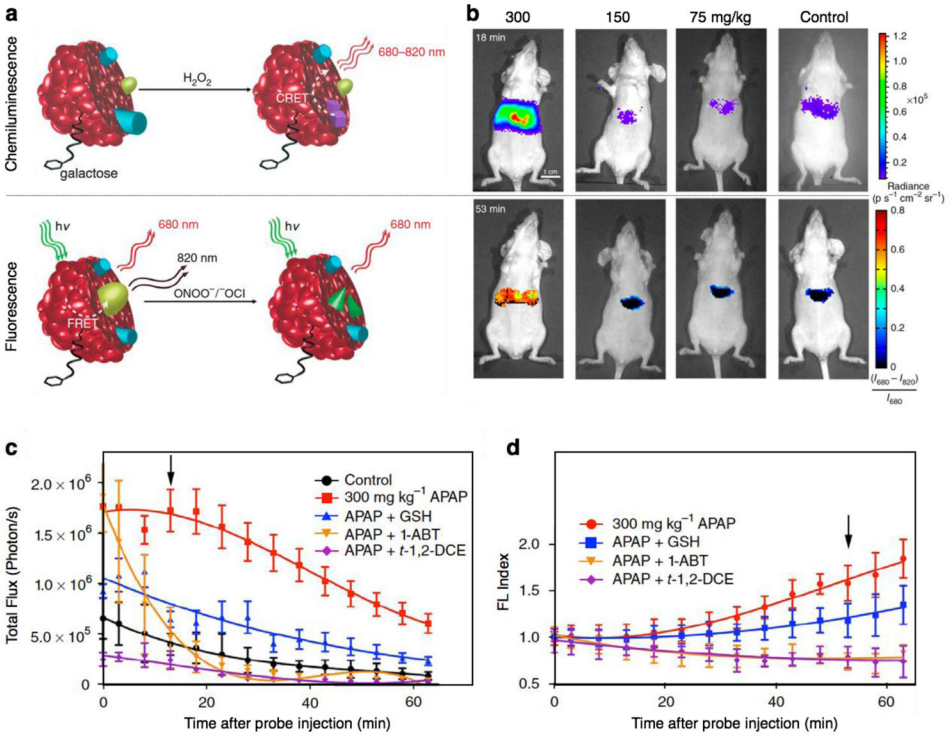

Fig. 6.

(**a**) Illustration of the mechanism of simultaneous and differential detection of $ONOO^-$ or ^-OCl and H_2O_2 by CRET/FRET-SPN. After drug challenge to the liver, the SPN report *via* the chemiluminescent and fluorescent channels the generation of radical metabolites at safe (left) and toxic (right) drug doses. (**b**) Real-time *in vivo* imaging of hepatotoxicity after acetaminophen administration to mice: Representative images of mice receiving acetaminophen or saline (control) intraperitoneally, followed by CRET/FRET-SPN (0.8 mg) intravenously. Chemiluminescence (top, imaged 18 min after nanoparticle administration) and fluorescence (bottom, imaged 53 min after nanoparticle administration) channels are shown (n = 3 mice per treatment group). (**c&d**) Longitudinal, *in vivo* monitoring of the remediation of APAP-induced hepatotoxicity with the enzyme inhibitors (1-ABT and *t*-1,2-DCE) and the antioxidant scavenger (GSH). Emission intensities of the liver for chemiluminescence (**c**) or fluorescence ratiometric (**d**) signals over times. Black arrows indicate the respective time points shown in b. Values are the mean ± s.d. for n = 3 mice. Reproduced from ref. 60.

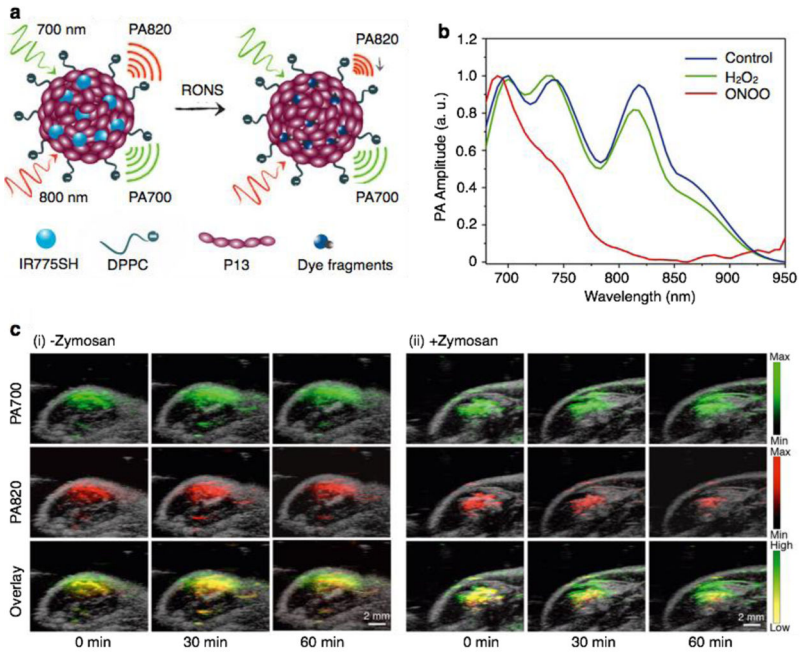

Fig. 7.

(**a**) Proposed RONS sensing mechanism of RSPN-P13. (**b**) Representative PA spectra of RSPN-P13 in the absence and presence of ROS. [RSPN-P13] = 5 μg/mL, [RONS] = 5 μM. (**c**) PA/ultrasound overlaid images of saline-treated (i) and zymosan-treated (ii) regions in the thigh of living mice (n = 3). RSPN-P13 (3 μg in 50 μL) was intramuscularly injected into the thigh 20 min after zymosan treatment. Reproduced from ref. 109.

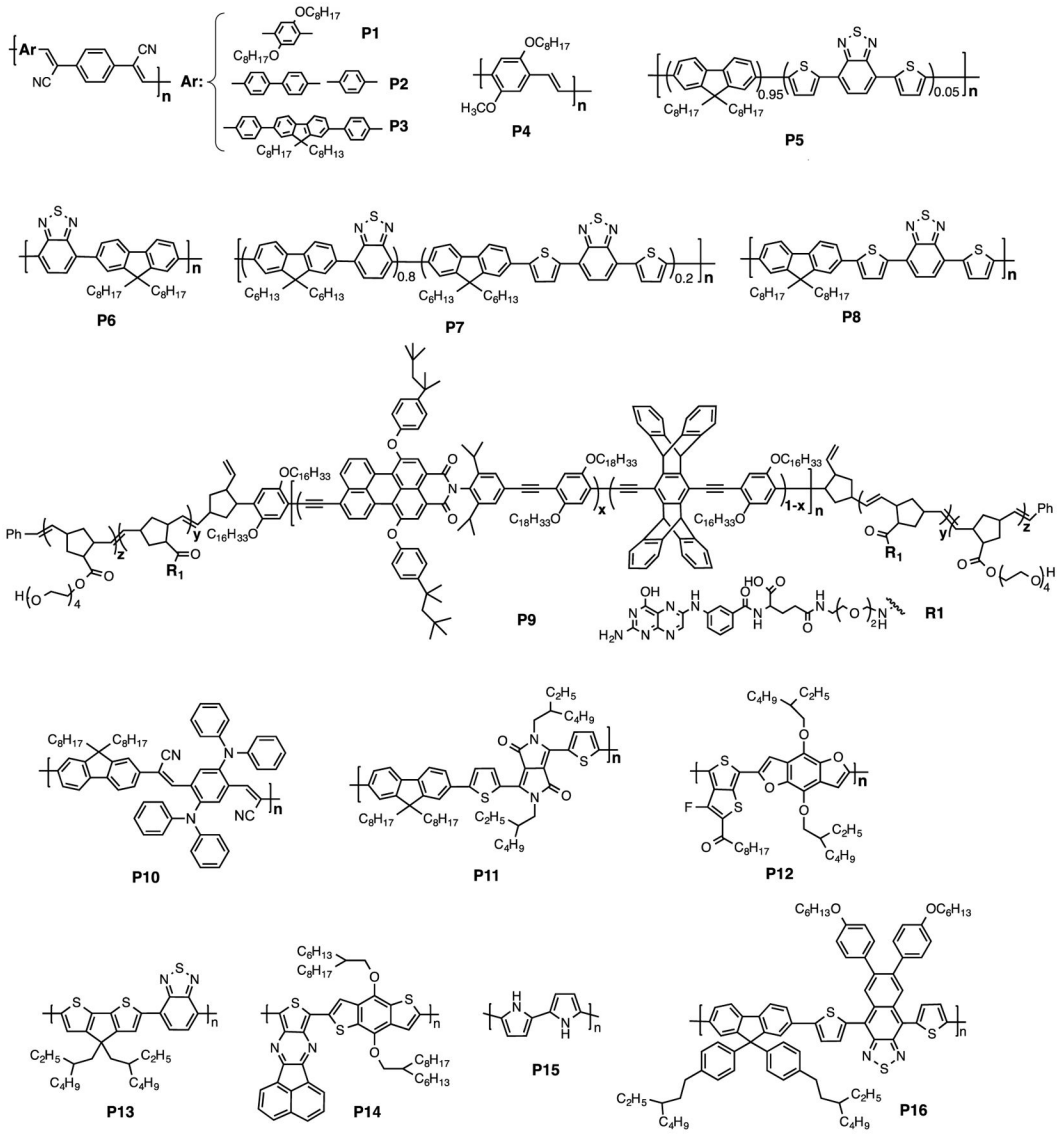

Scheme 1.
Chemical structures of some SPs used for imaging in living mice.

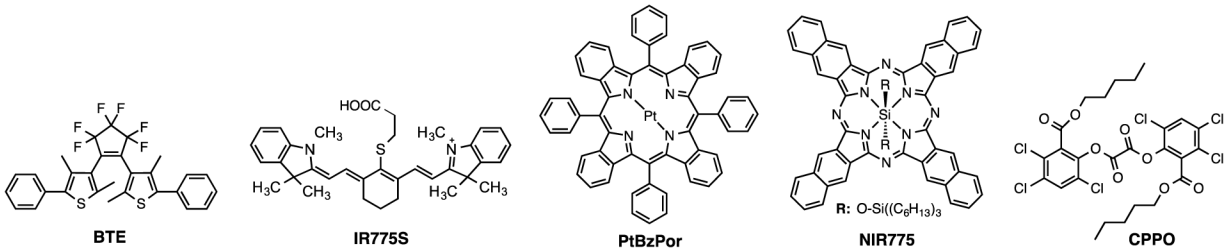

Scheme 2.

Chemical structures of organic molecules used for the preparation of SPNs.